POLITECNICO DI TORINO
Repository ISTITUZIONALE

Evaluation of the accuracy of classical beam FE models via locking-free hierarchically refined elements

(Article begins on next page)

25 April 2024

Evaluation of the accuracy of classical beam FE models via locking-free hierarchically refined elements

Erasmo Carrera[*], Alfonso Pagani[†]

Department of Mechanical and Aerospace Engineering, Politecnico di Torino,
Corso Duca degli Abruzzi 24, 10129 Torino, Italy.

Author for correspondence:
E. Carrera, Professor of Aerospace Structures and Aeroelasticity,
Department of Mechanical and Aerospace Engineering,
Politecnico di Torino,
Corso Duca degli Abruzzi 24,
10129 Torino, Italy,
tel: +39 011 090 6836,
fax: +39 011 090 6899,
e-mail: erasmo.carrera@polito.it

---

[*]Professor of Aerospace Structures and Aeroelasticity, e-mail: erasmo.carrera@polito.it
[†]Research Assistant, e-mail: alfonso.pagani@polito.it

Abstract

It is well known that the classical 6-DOF (Degrees of Freedom) beam theories that are incorporated in commercial finite element (FE) tools are not able to foresee higher-order phenomena, such as elastic bending/shear coupling, restrained torsional warping and three-dimensional strain effects. In this work, the accuracy of one-dimensional (1D) finite elements based on the classical theories (Euler-Bernoulli and Timoshenko theories as well as a 6-DOF model including torsion) is evaluated for a number of problems of practical interest and modelling guidelines are given. The investigation is carried out by exploiting a novel hierarchical, locking-free, finite beam element based on the well-known Carrera Unified Formulation (CUF). Thanks to CUF, the FE arrays of the novel beam element are written in terms of fundamental nuclei, which are invariant with respect to the theory approximation order. Thus, results from classical as well as arbitrarily refined beam models can be formally obtained by the same CUF beam element. Linear Lagrange shape functions are used in this paper to interpolate the generalized unknowns and shear locking phenomena are avoided by adopting a MITC (Mixed Interpolation of Tensorial Components) scheme. Different sample problems are addressed, including rectangular and warping-free circular cross-sections as well as thin-walled beams. The results from classical theories and the 6-DOF model are compared to those from higher-order refined beam models, both in terms of displacement and stress fields for various loading conditions. The discussion focuses on the limitations of the commonly used 1D FEs and the need for refined kinematics beams for most of the problems of common interest. The research clearly depicts CUF as a valuable framework to assess FE formulations such as the 6-DOF model herein considered, which is one of the most known and used finite element for the analysis of structures.

Keywords: Refined beam theories, 6-DOF beam element, Finite elements, MITC, Carrera unified formulation.

1 Introduction

One of the reasons for the success of the Finite Element Method (FEM) in solid mechanics is due to the use of 6-DOF (Degrees of Freedom) models into commercial tools. This choice, formerly adopted by Nastran codes, allows, in fact, the analysts to deal with only physical unknown quantities (e.g., translations and rotations in displacement-based formulations for pure mechanical problems). Moreover, mathematical models of complex structures can be straightforwardly constructed by assembling finite elements of different type and orientation, see for example the reinforced shell-like structures for aerospace applications [1]. Nevertheless, it is clear that limiting the maximum number of DOF per node can introduce certain physical inconsistencies. For this reason, most of the commercially available FEM software tools makes use of fictitious corrections, such as shear and warping correction factors (see for example [2]). Over the years, many scientists have been working on improved theories to overcome the limitations of classical models. However, their research, besides a few cases, rarely influenced the development of the commercial tools because of the aforementioned limitation of the 6-DOF per node. For the sake of completeness, a brief and not comprehensive review of higher-order theories is provided in the following. The attention is mainly focussed on beam modelling, which represents the principal subject of the proposed work.

Several examples of refined beam models can be found in well-known books on the theory of elasticity, for example, the book by Novozhilov [3]. A possible grouping of the methodologies developed to build higher-order beam theories could be the following: (i) the use of warping functions; (ii) the Saint-Venant based 3D solutions and the Proper Generalized Decomposition method (PGD); (iii) the Variational Asymptotic Method (VAM); (iv) and the Generalized Beam Theory (GBT). The introduction of warping functions to improve the displacement field of beams is a well-known strategy. Warping functions were first introduced in the framework of the Saint-Venant torsion problem [4, 5, 6]. Some of the earliest contributions to this approach were those by Umanskij [7], Vlasov [8] and Benscoter [9]. The Saint-Venant solution has been the theoretical basis of many advanced beam models. Three-dimensional elasticity equations were reduced to beam-like structures by Ladevèze and his co-workers [10]. Using this approach, a beam model can be built as the sum of a Saint-Venant part and a residual part and then applied to thick beams and thin-walled sections. The PGD for structural mechanics was first introduced in [11]. The PGD can be considered as a powerful tool to reduce the numerical complexity of a 3D problem. Bognet *et al.* [12] applied PGD to plate/shell problems, whereas Vidal *et al.* [13] extended PGD to beams. Asymptotic methods represent a powerful tool to develop structural models. In the beam model scenario, the works by Berdichevsky [14] and Berdichevsky *et al.* [15] were among the earliest contributions that exploited the VAM. These works introduced an alternative approach to constructing refined beam theories in which a characteristic parameter (e.g., the cross-section thickness of a beam) is exploited to build an asymptotic series. Those terms that exhibit the same order of magnitude as the parameter when it vanishes are retained. Some valuable contributions on asymptotic methods are those related to VABS models, as in Volovoi *et al.* [16]. The GBT has been derived from Schardts work [17, 18]. The GBT enhances classical

theories by exploiting a piece-wise description of thin-walled sections. It has been employed extensively and extended, in various forms, by Silvestre and Camotim, and their co-workers (see for example [19]). Many other higher-order theories, based on enhanced displacement fields over the beam cross-section, have been introduced to include non-classical effects. Some considerations on higher-order beam theories were made by Washizu [20]. Other refined beam models can be found in the excellent review by Kapania and Raciti [21, 22], which focused on bending, vibration, wave propagations, buckling and post-buckling. For further details about beam models, the reader is also referred to [23].

Most of the refined theory in the literature are problem dependent. Conversely, according to the well-known Carrera Unified Formulation (CUF), higher-order kinematics can be hierarchically developed in an automatic manner (see [24]). Regarding beam theories, CUF has been successfully applied to thin-walled structures [25, 26], buckling problems [27], free vibration and dynamic response analyses [28, 29], composite structures [30, 31] and component-wise analysis of aerospace and civil structures [32, 33]. The principal characteristic of CUF models is that the order of the theory is a free parameter, or an input, of the analysis. Hence, in a FEM framework, classical and arbitrarily refined elements can be formally developed by using the same formulation. This makes CUF a valuable tool to evaluate the accuracy of any structural model in a unified manner, see for example [32, 34]. This property of CUF is therefore exploited in the present paper, whose aim is to assess the accuracy of classical finite beam elements, such as those based on the Euler-Bernoulli Beam Model (EBBM), the Timoshenko Beam Model (TBM), and the 6-DOF beam model including twisting. In fact, a two-node, locking-free, CUF finite beam element is developed in the following and used to obtain classical and refined results of compact and thin-walled cross-section beam structures undergoing various loading conditions.

Shear locking phenomena are overcome in this work by adopting an MITC (Mixed Interpolation of Tensorial Components) technique, see [35, 36, 37]. The MITC formulation allows the transverse shear locking phenomenon to be eliminated by introducing an independent finite element approximation into the element domains for the transverse shear strains.

This work is organized as follows: (i) first, classical beam theories are formulated in the framework of CUF; (ii) higher-order models are then developed by approximating the beam kinematics via arbitrarily truncated expansion series; (iii) next, an MITC finite element formulation is outlined in Section 4; (iv) subsequently, the novel beam element is used to analyse various problems and the results of classical beam elements are compared to those from higher-order models; (v) finally, some comments and guidelines are discussed.

2   Classical beam theories

Figure 1 shows a generic beam and the Cartesian coordinate system adopted. The beam is depicted with a rectangular cross-section. However, this choice does not affect the validity of the proposed formulation. The
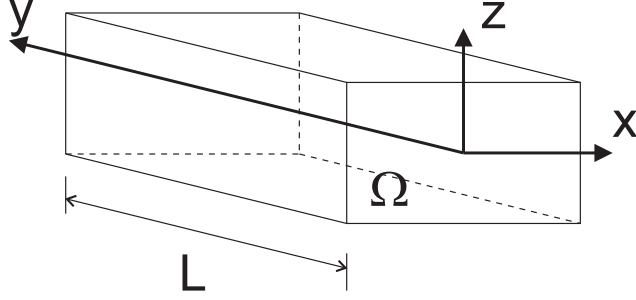
Figure 1: Coordinate frame of the reference beam

kinematic field of the Euler-Bernoulli Beam Model (EBBM) can be written as

$$
\begin{aligned}
u_x &= u_{x1} \\
u_y &= u_{y1} - x\,\frac{\partial u_{x1}}{\partial y} + z\,\frac{\partial u_{z1}}{\partial y} \\
u_z &= u_{z1}
\end{aligned}
\tag{1}
$$

where u_x, u_y and u_z are the displacement components of a point belonging to the beam domain along x, y and z, respectively; u_{x1}, u_{y1} and u_{z1} are the displacements of the beam axis; $-\dfrac{\partial u_{x1}}{\partial y}$ and $\dfrac{\partial u_{z1}}{\partial y}$ are the rotations of the cross-section about the z- (i.e. ϕ_z) and x-axis (i.e. ϕ_x). According to EBBM, the deformed cross-section remains plane and orthogonal to the beam axis because cross-sectional shear deformation phenomena are neglected. Shear stresses play a significant role in several problems (e.g., short beams and composite structures), and their neglect can lead to incorrect results. One may want to generalize Eq. (1) and overcome the EBBM assumption of the orthogonality of the cross-section. The improved displacement field results in the Timoshenko Beam Model (TBM),

$$
\begin{aligned}
u_x &= u_{x1} \\
u_y &= u_{y1} + x\,\phi_z - z\,\phi_x \\
u_z &= u_{z1}
\end{aligned}
\tag{2}
$$

TBM constitutes an improvement over EBBM, because the cross-section does not necessarily remain perpendicular to the beam axis after deformation, and two degrees of freedom (i.e. the unknown rotations, ϕ_z and ϕ_x) are added to the original displacement field.

In this paper, particular attention is given to a 6-DOF model, i.e. a TBM model including torsion. The resulting kinematic foresees first-order shear effects and twisting.

$$
\begin{aligned}
u_x &= u_{x1} + z\phi_y \\
u_y &= u_{y1} + x\,\phi_z - z\,\phi_x \\
u_z &= u_{z1} - x\phi_y
\end{aligned}
\tag{3}
$$

where ϕ_y represents the rigid rotation of the beam cross-section about the y-axis.

3 Higher-order, hierarchical models by CUF

Classical beam models grant reasonably good results when slender, solid section, homogeneous structures are considered. On the other hand, the analysis of short, thin-walled, open cross-section beams may require more sophisticated theories to achieve sufficiently accurate results, see [3]. As briefly discussed in Section 1, many refined beam theories have been proposed over the last century to overcome the limitations of classical beam modelling. As a general guideline, it is clear that the richer the kinematic field, the more accurate the 1D model becomes [20].

In the framework of the Carrera Unified Formulation (CUF), the number of terms in the kinematic field is arbitrary. In a compact form, the kinematics of a CUF beam model can be summarized as

$$\mathbf{u}(x, y, z) = F_\tau(x, z)\mathbf{u}_\tau(y), \qquad \tau = 1, 2, ..., M \tag{4}$$

where $\mathbf{u} = \{u_x\, u_y\, u_z\}^{\mathrm{T}}$ is the transposed displacement vector; F_τ are generic functions of the coordinates x and z on the cross-section; $\mathbf{u}_\tau$ is the vector of the *generalized displacements* laying on the beam axis; M stands for the number of terms used in the expansion; and τ represents summation. In this paper, we use Taylor-like expansion series polynomials as F_τ functions; i.e., 2D polynomials $x^i z^j$ (i and j are positive integers) are employed as basis functions to generate beam theories. This class of hierarchical CUF models has been denoted as TE (Taylor-Expansion) in the literature, see for example [38, 39, 28]. It should be noted that Eqs. (1) to (3) are particular cases of the linear ($N = 1$) TE model, which can be expressed as

$$
\begin{aligned}
u_x &= u_{x_1} + x\, u_{x_2} + z\, u_{x_3} \\
u_y &= u_{y_1} + x\, u_{y_2} + z\, u_{y_3} \\
u_z &= u_{z_1} + x\, u_{z_2} + z\, u_{z_3}
\end{aligned}
\tag{5}
$$

where the parameters on the right-hand side (u_{x_1}, u_{y_1}, u_{z_1}, u_{x_2}, etc.) are the displacements of the beam axis and their first derivatives. In other words, the linear ($N = 1$) TE model makes use of the following cross-sectional functions:

$$
\begin{aligned}
F_{1_x} &= F_{1_y} = F_{1_z} = 1 \\
F_{2_x} &= F_{2_y} = F_{2_z} = x \\
F_{3_x} &= F_{3_y} = F_{3_z} = z
\end{aligned}
\tag{6}
$$

Conversely, in the case of the 6-DOF beam model that is of particular interest in this paper, the following F_τ functions are used:

$$
\begin{aligned}
F_{1_x} &= F_{1_y} = F_{1_z} = 1 \\
F_{2_x} &= 0,\ F_{2_y} = -F_{2_z} = x \\
F_{3_x} &= -F_{3_y},\ F_{3_z} = 0
\end{aligned}
\tag{7}
$$

More details about TE models and the formulation of classical models as particular cases of TE can be found

in [40]. Nevertheless, it is interesting to underline that higher-order TE beam models can be automatically generated by increasing the number of expansion terms M. For example, the third-order ($N = 3$) TE model can be expressed as

$$
\begin{aligned}
u_x &= u_{x_1} + x\, u_{x_2} + z\, u_{x_3} + x^2\, u_{x_4} + xz\, u_{x_5} + z^2\, u_{x_6} + x^3\, u_{x_7} + x^2 z\, u_{x_8} + xz^2\, u_{x_9} + z^3\, u_{x_{10}} \\
u_y &= u_{y_1} + x\, u_{y_2} + z\, u_{y_3} + x^2\, u_{y_4} + xz\, u_{y_5} + z^2\, u_{y_6} + x^3\, u_{y_7} + x^2 z\, u_{y_8} + xz^2\, u_{y_9} + z^3\, u_{y_{10}} \\
u_z &= u_{z_1} + x\, u_{z_2} + z\, u_{z_3} + x^2\, u_{z_4} + xz\, u_{z_5} + z^2\, u_{z_6} + x^3\, u_{z_7} + x^2 z\, u_{z_8} + xz^2\, u_{z_9} + z^3\, u_{z_{10}}
\end{aligned}
\tag{8}
$$

In this work, a CUF beam element is implemented according to Eq. (4) and results from classical beam theories as well as higher-order models are easily obtained with the same FE model by opportunely varying the expansion order N (i.e., the number of expansion terms M) and the F_τ functions, which are analysis input parameters.

4 Finite element formulation

4.1 Preliminaries

Strain and stress vectors, $\boldsymbol{\epsilon}$ and $\boldsymbol{\sigma}$, are grouped in bending components and in-plane shear components; respectively

$$
\begin{aligned}
\boldsymbol{\epsilon}_B &= \{\epsilon_{yy}\ \epsilon_{xx}\ \epsilon_{zz}\ \epsilon_{xz}\}^{\mathrm{T}}, \qquad \boldsymbol{\epsilon}_S = \{\epsilon_{yz}\ \epsilon_{xy}\}^{\mathrm{T}} \\
\boldsymbol{\sigma}_B &= \{\sigma_{yy}\ \sigma_{xx}\ \sigma_{zz}\ \sigma_{xz}\}^{\mathrm{T}}, \quad \boldsymbol{\sigma}_S = \{\sigma_{yz}\ \sigma_{xy}\}^{\mathrm{T}}
\end{aligned}
\tag{9}
$$

In the case of small displacements with respect to a characteristic dimension in the plane of Ω, the strain-displacement relations are

$$
\begin{aligned}
\boldsymbol{\epsilon}_B &= \mathbf{D}_B \mathbf{u} = \left(\mathbf{D}_{B_y} + \mathbf{D}_{B_\Omega}\right) \mathbf{u} \\
\boldsymbol{\epsilon}_S &= \mathbf{D}_S \mathbf{u} = \left(\mathbf{D}_{S_y} + \mathbf{D}_{S_\Omega}\right) \mathbf{u}
\end{aligned}
\tag{10}
$$

where

$$
\mathbf{D}_{B_y} = \begin{bmatrix} 0 & \partial_y & 0 \\ 0 & 0 & 0 \\ 0 & 0 & 0 \\ 0 & 0 & 0 \end{bmatrix}, \qquad
\mathbf{D}_{B_\Omega} = \begin{bmatrix} 0 & 0 & 0 \\ \partial_x & 0 & 0 \\ 0 & 0 & \partial_z \\ \partial_z & 0 & \partial_x \end{bmatrix}
$$

$$
\mathbf{D}_{S_y} = \begin{bmatrix} 0 & 0 & \partial_y \\ \partial_y & 0 & 0 \end{bmatrix}, \qquad
\mathbf{D}_{S_\Omega} = \begin{bmatrix} 0 & \partial_z & 0 \\ 0 & \partial_x & 0 \end{bmatrix}
\tag{11}
$$

In Eq. (11) $\partial_x = \frac{\partial}{\partial_x}$, $\partial_y = \frac{\partial}{\partial_y}$, and $\partial_z = \frac{\partial}{\partial_z}$. Constitutive laws are now employed to obtain stress components to give

$$
\begin{aligned}
\boldsymbol{\sigma}_B &= \tilde{\mathbf{C}}_{BB} \boldsymbol{\epsilon}_B + \tilde{\mathbf{C}}_{BS} \boldsymbol{\epsilon}_S \\
\boldsymbol{\sigma}_S &= \tilde{\mathbf{C}}_{SB} \boldsymbol{\epsilon}_B + \tilde{\mathbf{C}}_{SS} \boldsymbol{\epsilon}_S
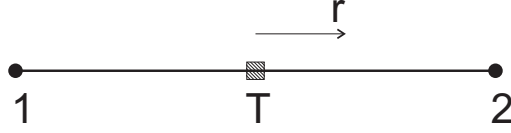\end{aligned}
\tag{12}
$$

Figure 2: Two-node MITC element and the related natural coordinate system

where matrices $\tilde{\mathbf{C}}_{BB}$, $\tilde{\mathbf{C}}_{BS}$, $\tilde{\mathbf{C}}_{SB}$, and $\tilde{\mathbf{C}}_{SS}$ contains the material coefficients. In the general case of orthotropic material, one has

$$
\tilde{\mathbf{C}}_{BB} = \begin{bmatrix} \tilde{C}_{33} & \tilde{C}_{23} & \tilde{C}_{13} & 0 \\ \tilde{C}_{23} & \tilde{C}_{22} & \tilde{C}_{12} & 0 \\ \tilde{C}_{13} & \tilde{C}_{12} & \tilde{C}_{11} & 0 \\ 0 & 0 & 0 & \tilde{C}_{44} \end{bmatrix}, \quad \tilde{\mathbf{C}}_{BS} = \tilde{\mathbf{C}}_{SB}^{\mathrm{T}} \begin{bmatrix} 0 & \tilde{C}_{36} \\ 0 & \tilde{C}_{26} \\ 0 & \tilde{C}_{16} \\ \tilde{C}_{45} & 0 \end{bmatrix}, \quad \tilde{\mathbf{C}}_{SS} = \begin{bmatrix} \tilde{C}_{55} & 0 \\ 0 & \tilde{C}_{66} \end{bmatrix} \tag{13}
$$

Coefficients $\tilde{C}_{ij}$ depend on the Young modulus, the Poisson ratio, and fiber orientation angle. For the sake of brevity, the expressions for the material coefficients are not reported here, but they can be found in standard texts, see for example [41, 42]. Classical theories and first-order models ($N = 1$) require the necessary assumption of reduced material stiffness coefficients to correct Poisson's locking (see [43]). In this paper, Poisson's locking is corrected according to the method outlined by Carrera *et al.* [40].

4.2   2-node MITC element

In this section, a 2-node MITC element based on CUF is formulated. The MITC2 element considered is shown in Fig. 2 along with the natural coordinate $r \in [-1, 1]$. According to FEM, the generalized displacements $\mathbf{u}_\tau(y)$ in Eq. (4) are interpolated by means of the shape functions N_i

$$
\mathbf{u}_\tau(y) = N_i(y)\mathbf{q}_{\tau i} \tag{14}
$$

where $\mathbf{q}_{\tau i} = \{q_{u_{x_{\tau i}}} \ q_{u_{y_{\tau i}}} \ q_{u_{z_{\tau i}}}\}^{\mathrm{T}}$ are the nodal generalized displacements and i indicates summation over the number of points of the beam element. In the case of the MITC2 beam element we use linear Lagrange shape functions that, in the natural reference system, can be expressed as

$$
N_1(r) = \frac{1}{2}(1 - r), \qquad N_2(r) = \frac{1}{2}(1 + r) \tag{15}
$$

In classical FEM techniques, both bending and shear strain components are computed from displacements by using geometrical relations (Eq. (14)). In particular, by substituting CUF (Eq. (4)) and FEM

approximation (Eq. (14)) into Eq. (10), one has

$$\begin{aligned}
\boldsymbol{\epsilon}_B &= F_\tau \left(\mathbf{D}_{B_y} N_i \mathbf{I} \right) \mathbf{q}_{\tau i} + \left(\mathbf{D}_{B_\Omega} F_\tau \mathbf{I} \right) N_i \mathbf{q}_{\tau i} \\
\boldsymbol{\epsilon}_S &= F_\tau \left(\mathbf{D}_{S_y} N_i \mathbf{I} \right) \mathbf{q}_{\tau i} + \left(\mathbf{D}_{S_\Omega} F_\tau \mathbf{I} \right) N_i \mathbf{q}_{\tau i}
\end{aligned} \tag{16}$$

where $\mathbf{I}$ is the 3×3 identity matrix. On the contrary, according to the MITC method, the in-plane shear strains are interpolated a-priori [44].

$$\overline{\boldsymbol{\epsilon}}_S = \overline{N}_m \boldsymbol{\epsilon}_{S_m} \tag{17}$$

where m indicates summation over the tying points (see [36]); $\overline{\boldsymbol{\epsilon}}_S$ is the assumed in-plane shear strains vector; $\boldsymbol{\epsilon}_{S_m}$ is the in-plane strains vector evaluated at the tying point m according to Eq. (16); and $\overline{N}_m$ are the assumed interpolation functions satisfying

$$\overline{N}_m^n = \delta_m^n, \qquad \delta_m^n = \begin{cases} 1 & \text{if } m = n \\ 0 & \text{otherwise} \end{cases} \tag{18}$$

where m and n go from 1 to the number of tying points within the element. In the case of the 2-node Lagrangian element as in this paper, only one single tying point is used to approximate the in-plane shear strains; thus, $m = 1$ and $\overline{N}_1$ assumes value 1 at the tying point T and it is equal to 0 in the remaining part of the domain. In other words, in the case of the MITC2 element, the shear strains vector $\overline{\boldsymbol{\epsilon}}_S$ is assumed a-priori to be constant along the element length and equal to the shear strains vector of Eq. (16) evaluated at the tying point T, which is graphically shown in Fig. 2. Formally,

$$\overline{\boldsymbol{\epsilon}}_S = \boldsymbol{\epsilon}_{S_T} \tag{19}$$

where $\boldsymbol{\epsilon}_{S_T} = \boldsymbol{\epsilon}_S(T)$. Equation (16) is now substituted into Eq. (19). It holds

$$\overline{\boldsymbol{\epsilon}}_S = F_\tau \left(\mathbf{D}_{S_y} N_i \mathbf{I} \right)_T \mathbf{q}_{\tau i} + \left(\mathbf{D}_{S_\Omega} F_\tau \mathbf{I} \right) N_{i_T} \mathbf{q}_{\tau i} \tag{20}$$

where N_{i_T} is the value of the i-th shape function of Eq. (15) assumed at the tying point T; i.e., $N_{i_T} = N_i(T)$ or $N_{i_T} = N_i(r = 0)$ in the natural coordinate system. Equivalently, $\left(\mathbf{D}_{S_y} N_i \mathbf{I} \right)_T$ is $\left(\mathbf{D}_{S_y} N_i \mathbf{I} \right) = \left(\mathbf{D}_{S_y} N_i(y) \mathbf{I} \right)$ evaluated at the tying point T.

Constitutive equations are also re-interpolated for the case of MITC elements. Indexes s and j are used

in the following instead of τ and i for the sake of convenience:

$$
\begin{aligned}
\overline{\boldsymbol{\sigma}}_B &= \tilde{\mathbf{C}}_{BB}\boldsymbol{\epsilon}_B + \tilde{\mathbf{C}}_{BS}\overline{\boldsymbol{\epsilon}}_S \\
&= \tilde{\mathbf{C}}_{BB}\left[F_s\left(\mathbf{D}_{B_y}N_j\mathbf{I}\right)\mathbf{q}_{sj} + \left(\mathbf{D}_{B_\Omega}F_s\mathbf{I}\right)N_j\mathbf{q}_{sj}\right] + \\
&\quad \tilde{\mathbf{C}}_{BS}\left[F_s\left(\mathbf{D}_{S_y}N_j\mathbf{I}\right)_T\mathbf{q}_{sj} + \left(\mathbf{D}_{S_\Omega}F_s\mathbf{I}\right)N_{j_T}\mathbf{q}_{sj}\right] \\
\overline{\boldsymbol{\sigma}}_S &= \tilde{\mathbf{C}}_{SB}\boldsymbol{\epsilon}_B + \tilde{\mathbf{C}}_{SS}\overline{\boldsymbol{\epsilon}}_S \\
&= \tilde{\mathbf{C}}_{SB}\left[F_s\left(\mathbf{D}_{B_y}N_j\mathbf{I}\right)\mathbf{q}_{sj} + \left(\mathbf{D}_{B_\Omega}F_s\mathbf{I}\right)N_j\mathbf{q}_{sj}\right] + \\
&\quad \tilde{\mathbf{C}}_{SS}\left[F_s\left(\mathbf{D}_{S_y}N_j\mathbf{I}\right)_T\mathbf{q}_{sj} + \left(\mathbf{D}_{S_\Omega}F_s\mathbf{I}\right)N_{j_T}\mathbf{q}_{sj}\right]
\end{aligned}
\tag{21}
$$

4.3 PVD and fundamental nuclei

The stiffness matrix and the loading vector of the MITC2 CUF element are obtained via the principle of virtual displacements (PVD), which in its general (static) form holds

$$
\delta L_{\text{int}} = \delta L_{\text{ext}}
\tag{22}
$$

where L_{int} stands for the strain energy; L_{ext} is the work of the external loads; and δ stands for the virtual variation. According to the MITC technique outlined above, the virtual variation of the strain energy is

$$
\delta L_{\text{int}} = \int_V \left(\delta\boldsymbol{\epsilon}_B^{\mathrm{T}}\overline{\boldsymbol{\sigma}}_B + \delta\overline{\boldsymbol{\epsilon}}_S^{\mathrm{T}}\overline{\boldsymbol{\sigma}}_S\right)\mathrm{d}V
\tag{23}
$$

where $V = \Omega \times L$ is the volume of the beam, Ω being the cross-section area and L the length of the structure as in Fig. 1. By substituting Eq. (21), Eq. (20), and $\boldsymbol{\epsilon}_B$ from Eq. (16) into Eq. (23), the internal work is expressed as

$$
\delta L_{\text{int}} = \delta\mathbf{q}_{\tau i}^{\mathrm{T}}\mathbf{K}^{\tau sij}\mathbf{q}_{sj}
\tag{24}
$$

where $\mathbf{K}^{\tau sij}$ is the 3×3 fundamental nucleus of the MITC2 elemental stiffness matrix. Its components are given in the following and they are referred to as $K_{(rc)}^{\tau sij}$, where r ($r = 1, 2, 3$) denotes the row number and c

denotes the column number ($c = 1, 2, 3$):

$$
\begin{aligned}
K_{(11)}^{\tau s i j} &= J^{ij} \lhd F_{\tau,x} \tilde{C}_{22} F_{s,x} \rhd_\Omega + J^{ij} \lhd F_{\tau,z} \tilde{C}_{44} F_{s,z} \rhd_\Omega + J^i N_{j,y_T} \lhd F_{\tau,x} \tilde{C}_{26} F_s \rhd_\Omega + \\
&\quad N_{i,y_T} J^j \lhd F_\tau \tilde{C}_{26} F_{s,x} \rhd_\Omega + N_{i,y_T} N_{j,y_T} \lhd F_\tau \tilde{C}_{66} F_s \rhd_\Omega \\[4pt]
K_{(12)}^{\tau s i j} &= J^{ij,y} \lhd F_{\tau,x} \tilde{C}_{23} F_s \rhd_\Omega + J^i N_{j_T} \lhd F_{\tau,x} \tilde{C}_{26} F_{s,x} \rhd_\Omega + J^i N_{j_T} \lhd F_{\tau,z} \tilde{C}_{45} F_{s,z} \rhd_\Omega + \\
&\quad N_{i,y_T} J^{j,y} \lhd F_\tau \tilde{C}_{36} F_s \rhd_\Omega + N_{i,y_T} N_{j_T} \lhd F_\tau \tilde{C}_{66} F_{s,x} \rhd_\Omega \\[4pt]
K_{(13)}^{\tau s i j} &= J^{ij} \lhd F_{\tau,x} \tilde{C}_{12} F_{s,z} \rhd_\Omega + J^{ij} \lhd F_{\tau,z} \tilde{C}_{44} F_{s,x} \rhd_\Omega + J^i N_{j,y_T} \lhd F_{\tau,z} \tilde{C}_{45} F_s \rhd_\Omega + \\
&\quad N_{i,y_T} J^j \lhd F_\tau \tilde{C}_{16} F_{s,z} \rhd_\Omega \\[4pt]
K_{(21)}^{\tau s i j} &= J^{i,yj} \lhd F_\tau \tilde{C}_{23} F_{s,x} \rhd_\Omega + J^{i,y} N_{j,y_T} \lhd F_\tau \tilde{C}_{36} F_s \rhd_\Omega + N_{i_T} J^j \lhd F_{\tau,x} \tilde{C}_{26} F_{s,x} \rhd_\Omega + \\
&\quad N_{i_T} J^j \lhd F_{\tau,z} \tilde{C}_{45} F_{s,z} \rhd_\Omega + N_{i_T} N_{j,y_T} \lhd F_{\tau,x} \tilde{C}_{66} F_s \rhd_\Omega \\[4pt]
K_{(22)}^{\tau s i j} &= J^{i,yj,y} \lhd F_\tau \tilde{C}_{33} F_s \rhd_\Omega + J^{i,y} N_{j_T} \lhd F_\tau \tilde{C}_{36} F_{s,x} \rhd_\Omega + N_{i_T} J^{j,y} \lhd F_{\tau,x} \tilde{C}_{36} F_s \rhd_\Omega + \\
&\quad N_{i_T} N_{j_T} \lhd F_{\tau,x} \tilde{C}_{66} F_{s,x} \rhd_\Omega + N_{i_T} N_{j_T} \lhd F_{\tau,z} \tilde{C}_{55} F_{s,z} \rhd_\Omega \\[4pt]
K_{(23)}^{\tau s i j} &= J^{i,yj} \lhd F_\tau \tilde{C}_{13} F_{s,z} \rhd_\Omega + N_{i_T} J^j \lhd F_{\tau,x} \tilde{C}_{16} F_{s,z} \rhd_\Omega + N_{i_T} J^j \lhd F_{\tau,z} \tilde{C}_{45} F_{s,x} \rhd_\Omega + \\
&\quad N_{i_T} N_{j,y_T} \lhd F_{\tau,z} \tilde{C}_{55} F_s \rhd_\Omega \\[4pt]
K_{(31)}^{\tau s i j} &= J^{ij} \lhd F_{\tau,x} \tilde{C}_{44} F_{s,z} \rhd_\Omega + J^{ij} \lhd F_{\tau,z} \tilde{C}_{12} F_{s,x} \rhd_\Omega + J^i N_{j,y_T} \lhd F_{\tau,z} \tilde{C}_{16} F_s \rhd_\Omega + \\
&\quad N_{i,y_T} J^j \lhd F_\tau \tilde{C}_{45} F_{s,z} \rhd_\Omega \\[4pt]
K_{(32)}^{\tau s i j} &= J^{ij,y} \lhd F_{\tau,z} \tilde{C}_{13} F_s \rhd_\Omega + J^i N_{j_T} \lhd F_{\tau,x} \tilde{C}_{45} F_{s,z} \rhd_\Omega + J^i N_{j_T} \lhd F_{\tau,z} \tilde{C}_{16} F_{s,x} \rhd_\Omega + \\
&\quad N_{i,y_T} N_{j_T} \lhd F_\tau \tilde{C}_{55} F_{s,z} \rhd_\Omega \\[4pt]
K_{(33)}^{\tau s i j} &= J^{ij} \lhd F_{\tau,x} \tilde{C}_{44} F_{s,x} \rhd_\Omega + J^{ij} \lhd F_{\tau,z} \tilde{C}_{11} F_{s,z} \rhd_\Omega + J^i N_{j,y_T} \lhd F_{\tau,x} \tilde{C}_{45} F_s \rhd_\Omega + \\
&\quad N_{i,y_T} J^j \lhd F_\tau \tilde{C}_{45} F_{s,x} \rhd_\Omega + N_{i,y_T} N_{j,y_T} \lhd F_\tau \tilde{C}_{55} F_s \rhd_\Omega
\end{aligned}
\tag{25}
$$

In Eq. (25) the comma denotes partial derivatives with respect to spatial coordinates x, y, or z; N_{i,y_T} is the derivative of the i-th shape function of Eq. (15) evaluated at the tying point T, i.e. $N_{i,y_T} = N_{i,y}(T)$; and

$$
\begin{aligned}
&\lhd(...)\rhd_\Omega = \int_\Omega (...) \mathrm{d}x \mathrm{d}z, \\[6pt]
&\left(J^i, J^{i,y}, J^{ij}, J^{i,yj}, J^{ij,y}, J^{i,yj,y}\right) = \int_L \left(N_i, N_{i,y}, N_i N_j, N_{i,y} N_j, N_i N_{j,y}, N_{i,y} N_{j,y}\right) \mathrm{d}y
\end{aligned}
\tag{26}
$$

The fundamental nucleus $\mathbf{K}^{\tau s i j}$ has to be expanded versus the indexes $i, j = 1, 2$ and $\tau, s = 1, ..., M$ in order to obtain the MITC2, locking-free, elemental stiffness matrix of any beam theory desired. In fact, thanks to the hierarchical capabilities of CUF, any-order beam model can be easily coded by nesting the above nine components in four loop cycles and by choosing an appropriate set of cross-sectional functions F_τ. The elemental stiffness matrices are then assembled in the classical way of FEM to obtain the global stiffness matrix, see for example [24]. The fundamental nucleus $\mathbf{K}^{\tau s i j}$ of the CUF MITC2 element allows to easily investigate the accuracy of classical finite beam elements such as those incorporated in commercial FE tools, because classical to refined beam elements can be automatically developed.

11

The fundamental nucleus of the loading vector which is variationally coherent with the model can be obtained by introducing CUF and FEM approximation in the expression of the virtual variation of the work of the external loads, δL_{ext}. The derivation of the load vector is not derived here, but it can be found in [40], where more details about TE models are also given.

5 Numerical Results

The proposed hierarchical, locking-free element is assessed in this section and, then, used to investigate the limitations of classical models when applied to problems of practical interest. First, a simple square cross-section beam is considered: Convergence analyses and the capability of the present element to overcome shear-locking are briefly discussed. The attention is subsequently focussed on the higher-order features of the present CUF beam model and on the inefficacy of the classical models, such as the 6-DOF formulation. The discussion is argued by considering various loading conditions and geometries, including circular and thin-walled section beams.

5.1 Square cross-section beam

A cantilever square cross-section beam was considered as the first assessment. The side of the cross-section, b, was equal to 0.2 m. The length-to-side ration was $L/b = 10$. The structure was made of an aluminium alloy with the following characteristics: Young modulus $E = 75$ GPa, Poisson ratio $\nu = 0.33$. In the first load case, a point load $F_z = 100$ N was applied at the free end and a convergence analysis versus the number of MITC2 elements was conducted. Figure 3 shows the vertical displacement component, u_z, at the tip for various mesh discretizations and beam theories. In particular, classical beam models (i.e., EBBM, TBM, and the 6-DOF beam model) and refined theories, including the third- ($N = 3$), fifth- ($N = 5$), and seventh-order ($N = 7$) TE models, are considered. The second-order ($N = 2$) TE model presents a convergence rate similar to those of higher-order models and it is not shown in the figure. The results highlight the slower convergence of the higher-order models. Nevertheless, 100 MITC2 elements are employed in the following analysis that ensured convergent solutions of refined beams for all the cases under consideration. On the contrary, just 20 MITC2 elements are used in the case of classical beam theories.

The same load case is also exploited to demonstrate one of the most important characteristic of the proposed MITC2 element. It is well known that, according to elasticity theory and simple equilibrium considerations, shear is constant along the beam axis for the problem considered. Table 1 compares the shear stress value by the 6-DOF beam model by various, well-known, FE integration schemes and MITC. The shear stress values at the clamped end, at the mid-span and at the free end are shown in the table. All the results reported in Table 1 were obtained by using 20 linear 2-node elements. It is clear that the present MITC2 technique, unlike full, reduced and selective reduced integration schemes (see [40]), is not affected by shear-locking and
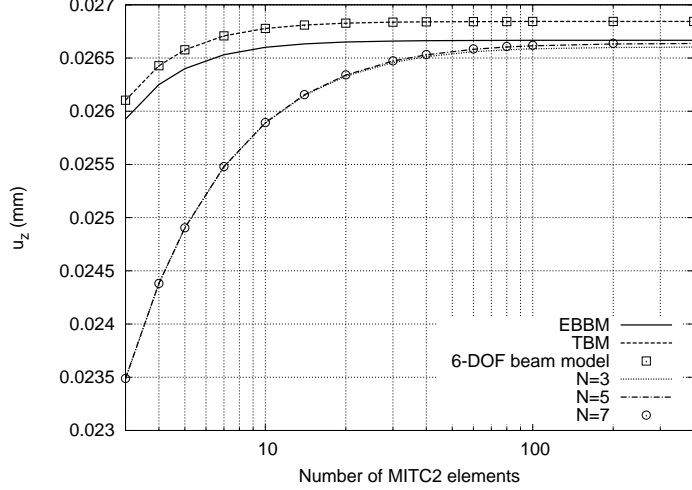
Figure 3: Vertical displacement at the tip of the square beam undergoing bending; Effect of the number of MITC2 elements on various beam models

	Full	Reduced	Selective reduced	MITC
$y = 0$	0.809	0.811	0.811	0.250
$y = L/2$	−0.337	−0.348	−0.348	0.250
$y = L$	0.247	0.247	0.247	0.250

Table 1: Shear stress component, $\sigma_{yz} \times 10^2$ (MPa), at various beam cross-sections by the 6-DOF beam model and various integration schemes; Square cross-section beam undergoing a point load
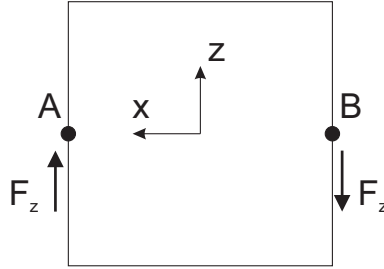

Figure 4: Tip cross-section of the square beam undergoing a torque load

it formally provides an exact interpolation for shear stress.

The attention is now focused on the investigation of the accuracy of classical FE beam elements. In the second load case, a torque was applied at the free end as shown in Fig. 4. The value of the force F_z that is applied at points A and B was as high as 50 N. Table 2 shows the vertical displacement component, u_z, at point A and the maximum value of the shear stress component, σ_{yz}, on the cross-section placed at $y = L/2$. The number of DOF for each FE model implemented is also given in the table. Classical and refined beam models obtained through MITC2 CUF elements are compared to an approximate analytical solution. In this paper, the analytical solution is found according to the following well-known relation [45]:

$$\theta = \frac{T\,L}{G\,J_t} \tag{27}$$

where θ is the twist angle, T is the applied torque, G is the shear modulus, and J_t is the torsional moment of

13

	$u_z \times 10^3$ (mm)	$\sigma_{yz} \times 10^3$ (MPa)	DOF
Anlt. Sol.	0.315	6.009	–
Classical and refined models via CUF			
EBBM	0	0	63
TBM	0	0	105
6-DOF	0.266	3.750	126
$N = 1$	0.271	3.750	189
$N = 2$	0.274	3.750	1818
$N = 3$	0.285	3.750	3030
$N = 4$	0.332	6.168	4545
$N = 5$	0.345	6.168	6363

Table 2: Vertical displacement at point A and maximum value of the shear stress at $y = L/2$; Square cross-section beam undergoing a torque load

inertia. An approximate formula is available for J_t in the case of square cross-section, $J_t \approx 0.1406\, b^4$. In fact, no exact expressions for the classical torsion constant are available for beams with non-circular cross-sections since warping phenomena occur. Once θ is computed, the vertical displacement at point A is evaluated as

$$u_z \approx \theta\, \frac{b}{2} \tag{28}$$

As far as the maximum shear stress is concerned, the following expression holds:

$$\sigma_{yz_{\max}} = \frac{T}{0.208\, b^3} \tag{29}$$

Figure 5 shows the distribution of the shear transverse stress on the mid-span cross-section. It is clear that at least a fourth-order ($N = 4$) beam model is necessary to detect warping phenomena for the case under consideration. For this particular analysis case, the 6-DOF beam model gives results similar to those from linear ($N = 1$) and third-order ($N = 3$) TE models.

In the last load case, the square cross-section beam was subjected to bending-torsion. Therefore, a single point load was applied at the tip cross-section as shown in Fig. 6. The value of the point load F_z was equal to 50 N. Table 3 shows the vertical displacements at points A and B (see Fig. 6) and the maximum value of the shear stress at the mid-span cross-section. The results are compared to those from classical analytical solutions. In the third row, in particular, the displacement by the pure bending beam theory is given according to the following Euler-Bernoulli expression:

$$u_{z_b} = \frac{F_z\, L^3}{3\, EI} \tag{30}$$

where I is the bending moment of inertia. To this solution, shear stress is obviously null. In the fourth row of Table 3, shear effects are added to Eq. (30)

$$u_{z_s} = \frac{F_z\, L}{A\, G} \tag{31}$$

(a) 6-DOF beam model

(b) $N = 1$
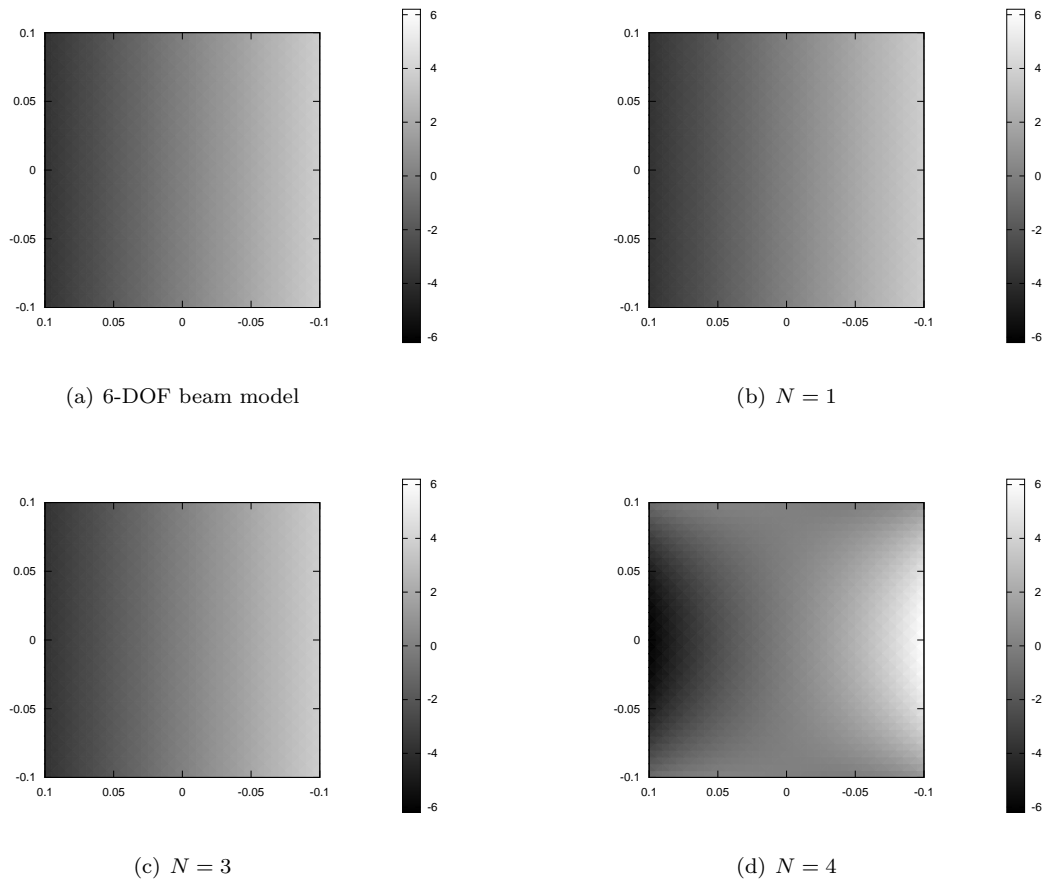
(c) $N = 3$

(d) $N = 4$

Figure 5: Distribution of the shear stress component, $\sigma_{yz} \times 10^3$ (MPa), on the mid-span cross-section; Square cross-section beam undergoing pure torsional load
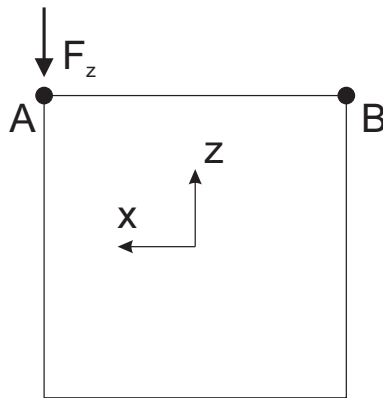

Figure 6: Tip cross-section of the square cross-section beam undergoing a bending/torsional load

	$-u_z \times 10^3$ @ point A (mm)	$-u_z \times 10^3$ @ point B (mm)	$-\sigma_{yz} \times 10^3$ (MPa)
Analytical solutions			
Pure bending case	1.333	1.333	0
Including bending shear	1.342	1.342	1.875
Including torsion	1.358	1.326	4.879
Classical and refined models via CUF			
EBBM	1.333	1.333	0
TBM	1.342	1.342	1.250
6-DOF	1.355	1.329	3.125
$N = 1$	1.382	1.355	3.125
$N = 2$	1.344	1.314	3.358
$N = 3$	1.350	1.316	4.008
$N = 4$	1.358	1.315	5.217
$N = 5$	1.363	1.315	5.271

Table 3: Vertical displacements at points A and B and maximum value of the shear stress at $y = L/2$; Square cross-section beam undergoing a bending-torsional load

where A is the area of the cross-section. In this case, the shear stress is given by the following formula:

$$\sigma_{yz_s}(z) = -\frac{F_z \, S_x(z)}{I \, b} \tag{32}$$

where $S_x(z)$ is the first moment of area. According to this analytical model, the maximum shear stress is at $z = 0$. It reads

$$\sigma_{yz_s}(z = 0) = -\frac{3 \, F_z}{2 \, A} \tag{33}$$

In the fifth column of Table 3, effects on displacement and shear components due to torsion are included according to Eqs. (27) to (29). For this problem, the number of DOF are the same as in the previous analysis case. It is noteworthy that EBBM and TBM are obviously unapplicable for the case under consideration. Conversely, the 6-DOF beam element provides good results in terms of displacements. On the other hand, accurate stress distribution analyses require the adoption for refined kinematics.

5.2 Circular cross-section beam

A cantilever circular cross-section beam was analyzed. The cross-section of the beam is shown in Fig. 7, together with the loading condition on the tip cross-section. The cross-section had radius R equal to 0.1 m. The length of the beam, load value (F_z), and material properties were equal to the square cross-section beam discussed in the previous example.

The vertical displacement at point A and the maximum value of the shear stress component at the mid-span cross-section is shown in Table 4. The results by classical and refined MITC2 CUF models are compared to an analytical solution as in the previous numerical example by using Eqs. (27) and (28). In the case of circular cross-section beam, the torsional moment of inertia is equal to $J_t = \frac{\pi R^4}{2}$. This value of the torsion constant is exact in the case that a plane section before rotating remains plane after rotating, and
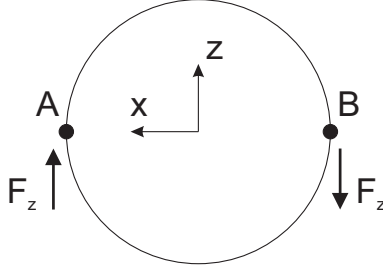
Figure 7: Tip cross-section of the circular beam undergoing a torque load

	$u_z \times 10^3$, mm	$\sigma_{yz} \times 10^3$, MPa
Anlt. Sol.	0.452	6.366
Classical and refined models via CUF		
EBBM	0	0
TBM	0	0
6-DOF	0.452	6.366
$N = 1$	0.459	6.366
$N = 2$	0.463	6.366
$N = 3$	0.487	6.366
$N = 4$	0.489	6.366
$N = 5$	0.508	6.366

Table 4: Vertical displacement at point A and maximum value of the shear stress at $y = L/2$; Circular cross-section beam undergoing a torque load

no local cross-sectional deformations occur. Those hypotheses are nearly true in the case of solid circular cross-section beams. Concerning the maximum value of the shear stress, it is computed according to the following expression:

$$\sigma_{yz_{\max}} = \frac{T R}{J_t} \tag{34}$$

Figures 8 and 9 show the cross-sectional distributions of shear stress component, σ_{yz}, and hoop displacement components. The results show that the 6-DOF model is able to detect analytical and higher-order solutions, because no warping phenomena are evident. Differences in the displacements by higher-order models are due to local cross-sectional deformations, which can be hierarchically detected by refining the beam model kinematics by CUF.

5.3 I-section beam

A doubly symmetric, I-shaped cross-section beam was further considered. The cross-section had a height $h = 100$ mm and a width $w = 96$ mm. The length to height ratio, L/h, was 10. The thickness of the flanges was $t_1 = 8$ mm, whereas the thickness of the web was $t_2 = 5$ mm. The material data were: elastic modulus $E = 200$ GPa and Poisson ratio, ν, equal to 0.29. A vertical force $F_z = -2 \times 10^3$ N was applied at point B (see Fig. 10) at the free end of the beam. The same problem was considered in [25], whose results are used hereinafter for comparison purpose.

Table 5 shows the vertical displacement at the loading point (point B) and at the tip cross-section centroid
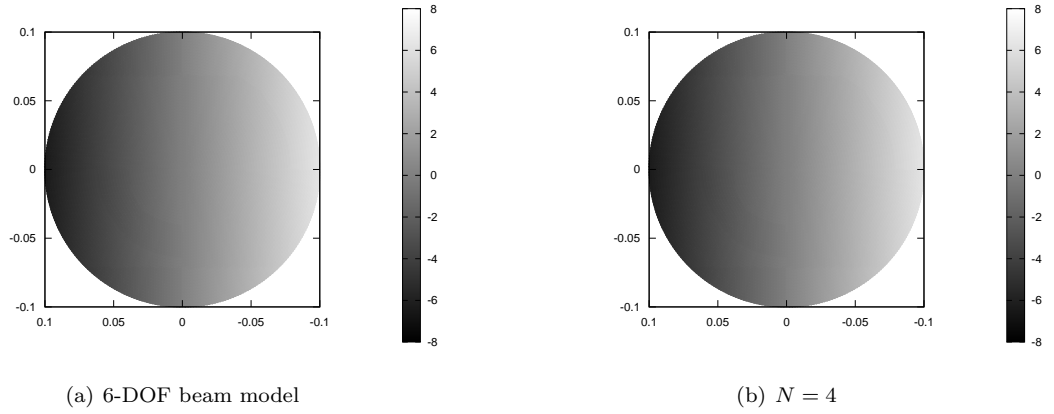
(a) 6-DOF beam model

(b) $N = 4$

Figure 8: Distribution of the shear stress component, $\sigma_{yz} \times 10^3$ (MPa), on the mid-span cross-section; Circular cross-section beam undergoing pure torsional load
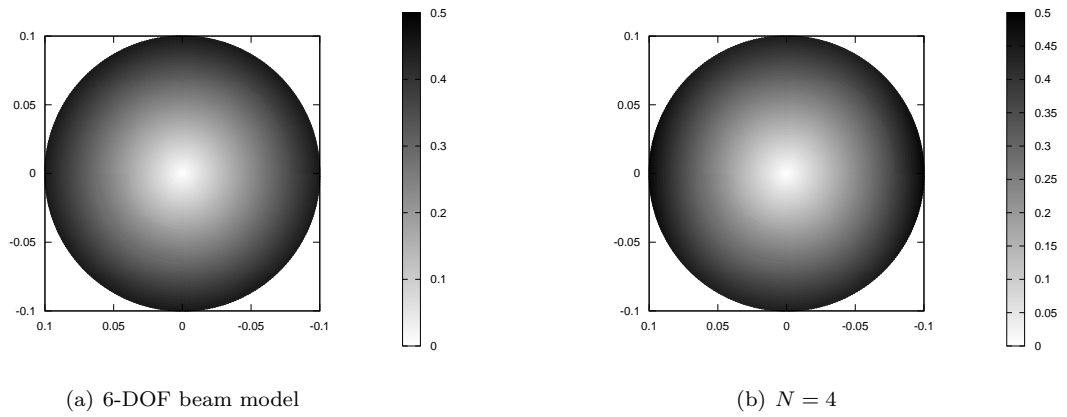

(a) 6-DOF beam model

(b) $N = 4$

Figure 9: Distribution of the cross-sectional displacement components, $\sqrt{u_x^2 + u_z^2} \times 10^3$ (mm), on the tip cross-section; Circular cross-section beam undergoing torsional load
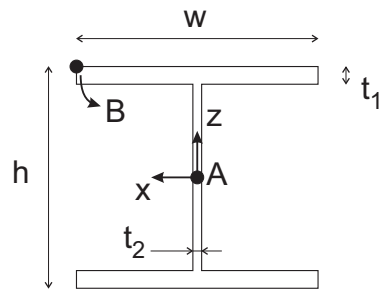

Figure 10: Tip cross-section of the I-section beam

	$-u_z$ @ point A (mm)	$-u_z$ @ point B (mm)	DOF
Reference solutions, [25]			
Multi-line	0.952	2.230	4185
Nastran 2D	1.006	2.437	61000
Nastran 3D	0.956	2.316	355800
Classical and refined models via MITC2 CUF elements			
EBBM	0.951	0.951	63
TBM	0.964	0.964	105
6-DOF	0.964	0.977	126
$N = 2$	0.957	0.976	1818
$N = 4$	0.991	1.257	4545
$N = 6$	0.994	1.361	8484
$N = 8$	0.997	1.649	13635
$N = 10$	1.000	1.687	19998
$N = 12$	1.000	2.002	27573
$N = 14$	1.001	2.418	36360

Table 5: Vertical displacements at points A and B; I-section beam undergoing a bending-torsional load
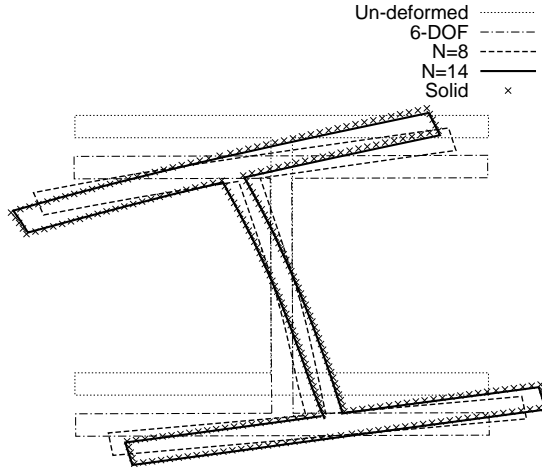

Figure 11: Deformed configuration of the tip cross-section by various models; I-section beam undergoing a bending-torsional load

(point A). The number of DOF for each model is also given. The results by the present classical and refined MITC2 CUF beam elements are compared to a multi-line model (see [25]) and to 2D and 3D MSC Nastran FEM models. The table and Fig. 11, which shows the tip cross-section deformation by various theories, demonstrate the inefficiency of classical models and that very higher-order kinematics are needed to detect the 3D in-plane strains for the case under consideration. Figures 12 and 13 compare stress distribution between the 6-DOF beam models and the solid model by Nastran. In particular, the axial stress distribution at $y = 0$ is compared in Fig. 12, whereas the in-plane shear stress σ_{yz} at the mid-span section is compared in Fig. 13. The results clearly show that, although the 6-DOF beam model can detect torsion, classical beam finite elements may produce non-negligible errors in the case of doubly-symmetric thin-walled structures that are not loaded at the centroid.
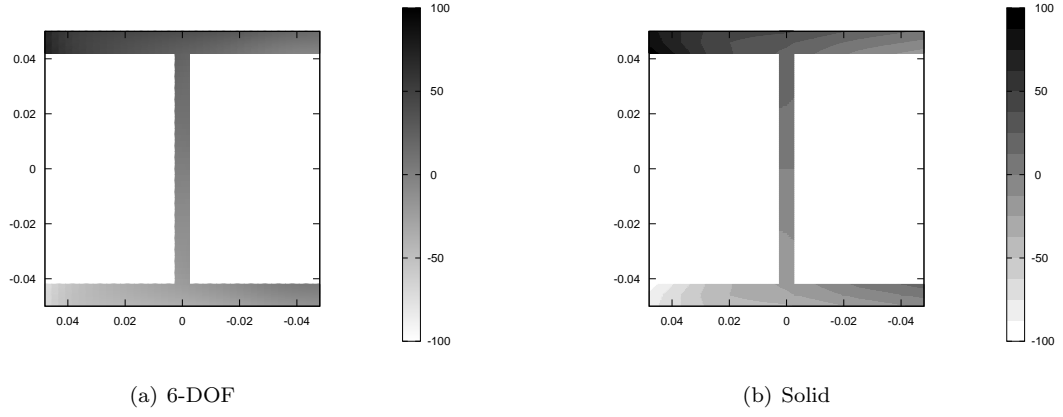
(a) 6-DOF   (b) Solid

Figure 12: Distribution of the axial stress component, σ_{yy} (MPa), on the clamped cross-section; I-section beam undergoing a bending-torsional load

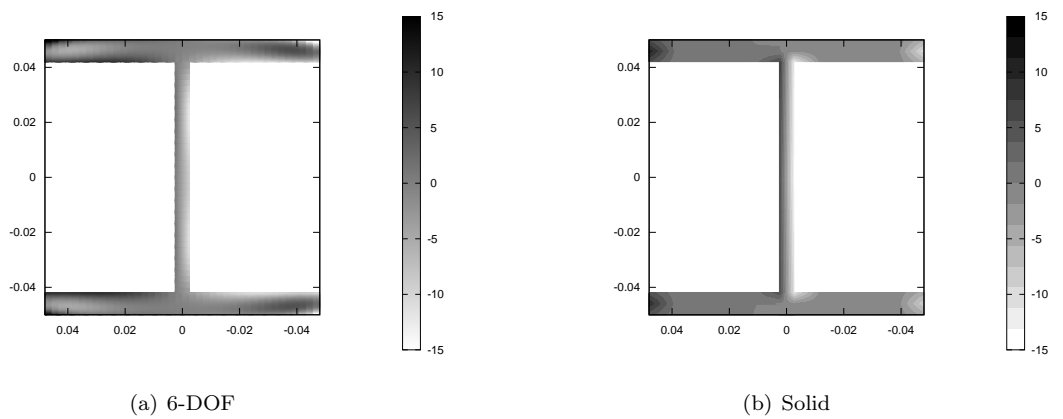(a) 6-DOF   (b) Solid

Figure 13: Distribution of the shear stress component, σ_{yz} (MPa), on the mid-span cross-section; I-section beam undergoing a bending-torsional load
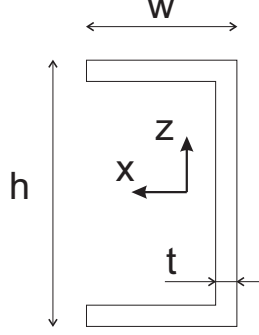
Figure 14: Tip cross-section of the C-section beam
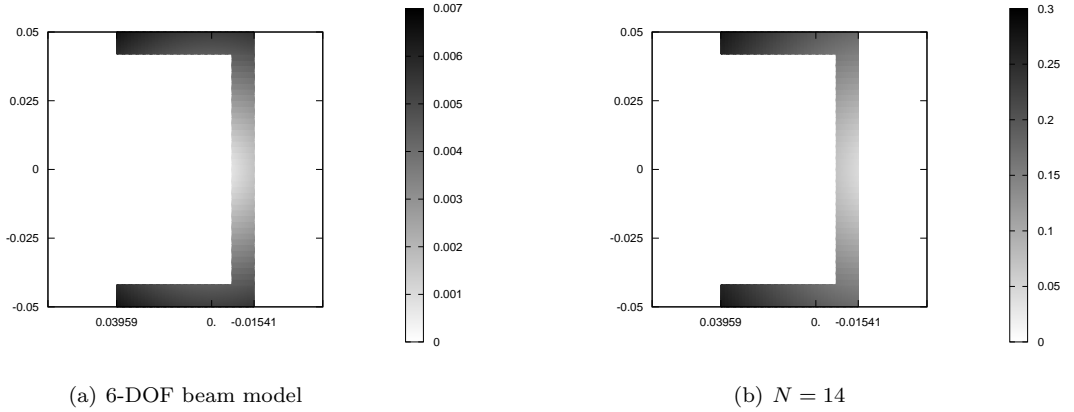

(a) 6-DOF beam model

(b) $N = 14$

Figure 15: Distribution of the hoop displacements, $\sqrt{u_x^2 + u_z^2}$ (mm), on the tip cross-section; C-section beam undergoing differential bending

5.4 C-section beam

In the last analysis case, a single-symmetric C-shaped cross-section beam was considered (see Fig. 14). The C-section beam had and height $h = 100$ mm and a width $w = 50$ mm. The beam was as long as 1 m. The thickness of the flanges was $t = 8$ mm. The structure was completely made of the same steel alloy as the I-section beam considered in the previous section.

Applying a pure torque to this kind of beams is not straightforward. Torque loads are most likely applied as differential bending loads in the reality. Thus, two forces were applied at the tip cross-section in correspondence of the horizontal flanges. In particular, a force $F_z = -200$ N was applied at the top flange, whereas a force equal to $-F_z$ was applied at the bottom flange. Figures 15 and 16 show the distributions of the hoop displacement (i.e. $\sqrt{u_x^2 + u_z^2}$) and the out-of-plane axial displacement, respectively. It is clear that the classical 6-DOF model is not able to detect the mechanical behaviour of the C-section beam undergoing the differential bending load. For example, warping is quantitatively non-negligible and higher-order models are mandatory to detect the 3D effects affecting the mechanical behaviour of the structures under consideration. Another interesting observation is related to the position of the shear (or twisting) centre, here literally denoted as the point, on the sectional symmetric axis, characterized by zero transverse shear strain ($\epsilon_{yz} = 0$). It is cleat that this point
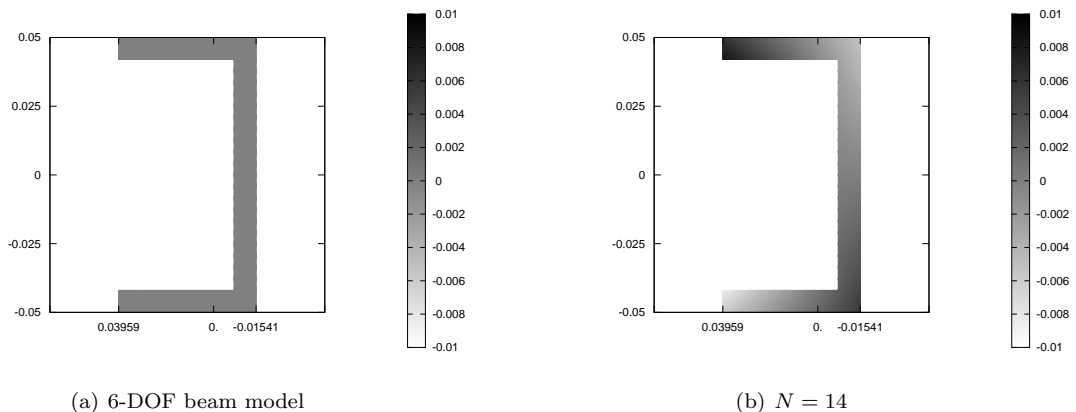
(a) 6-DOF beam model (b) $N = 14$

Figure 16: Distribution of the out-of-plane axial displacements, u_y (mm), on the tip cross-section; C-section beam undergoing differential bending

Model	e_x (mm)
Saint-Venant's theory	-28.66
MITC2 CUF elements	
EBBM	0.00
TBM	0.00
6-DOF	0.00
$N = 2$	-4.66
$N = 3$	-20.16
$N = 4$	-25.16
$N = 6$	-26.41

Table 6: Shear centre position at the tip cross-section for various models; C-section beam

on the cross-section depends on the stress distribution, i.e. on the model adopted. Figure 15 shows that in the case of the 6-DOF beam model the shear centre lays inside the C-section. Conversely, the shear centre translates outside the cross-section in the case of higher-order models. This aspect is further investigated through Table 6, which gives the x-coordinate of the shear centre with respect to the cross-section centroid for various beam elements and Saint-Venant's hypotheses. It is interesting to note that, according to classical beam elements, the shear centre correspond to the section centroid. At least a third-order ($N = 3$) kinematics (i.e., second-order approximation for strains/stresses) is needed to detect the position of the shear centre according to the Saint-Venant 3D elasticity solution.

6 Conclusions

In this paper, the accuracy of classical beam theories available in commercial FE codes has been investigated by using a hierarchical, locking-free beam element. The two-node element has been formulated by using the well-known Carrera Unified Formulation (CUF) and shear locking is overcome by employing an MITC (Mixed Interpolation of Tensorial Components) technique. The resulting beam element is a powerful tool that can be used for comparing various theories. In fact, CUF allows for the derivation of the finite element arrays (e.g.

the stiffness matrix) in terms of fundamental nuclei, whose formal expressions are invariant with respect to the theory order. Thus, results from classical theories (e.g. a 6-DOF beam element) and refined kinematics can be straightforwardly obtained with the same FE model by just changing a single input parameter (the beam order N). Various analysis cases and geometries have been considered in this work, and the results have suggested some interesting conclusions and guidelines about classical beam elements, such as

- A 6-DOF beam model including twisting and a first-order distribution of the shear stresses can be used for the analysis of circular compact cross-section beams with acceptable accuracy. In fact, this kind of beams is not subjected to constraint warping.

- Even in the simple case of square cross-sections, classical models are not suggested in the case of torsional or bending-torsional loads. In this cases, at least a fourth-order ($N = 4$) beam model is needed.

- Very rich displacement fields (e.g. $N = 14$) should be employed to detect 3D strains and cross-sectional displacements in the case of thin-walled structures.

- For some problems, the 6-DOF beam model can provide acceptable results in terms of displacements. However, accurate stress fields may require the adoption of recovery procedures from 3D equilibrium equations. The present MITC2 CUF beam element, on the other hand, already includes 3D elasticity relations and no post-processing for stress recovery is required once sufficiently enriched kinematics is adopted.

References

[1] E. Carrera, A. Pagani, and M. Petrolo. Classical, refined and component-wise theories for static analysis of reinforced-shell wing structures. *AIAA Journal*, 51(5):1255–1268, 2013. doi: 10.2514/1.J052331.

[2] S. P. Timoshenko. On the corrections for shear of the differential equation for transverse vibrations of prismatic bars. *Philosophical Magazine*, 41:744–746, 1922.

[3] V. V. Novozhilov. *Theory of Elasticity*. Pergamon Press, 1961.

[4] P. Ladevze and J. Simmonds. New concepts for linear beam theory with arbitrary geometry and loading. *European Journal of Mechanics - A/Solids*, 17(3):377–402, 1998.

[5] J. Lubliner. *Plasticity Theory*. Macmillan Publishers, London, 1990.

[6] I. S. Sokolnikoff. *Mathematical Theory of Elasticity*. McGraw-Hill, New York, 1956.

[7] A.A. Umanskij. *Kručenije i izgib tonkostennykh aviokon-strukcij*. Oborongiz, Moskva, 1939. (in Russian).

[8] V. Z. Vlasov. *Thin-walled elastic beams*. National Science Foundation, Washington, 1961.

[9] S. Benscoter. A theory of torsion bending for multicell beams. *Journal of Applied Mechanics*, 21(1):25–34, 1954.

[10] P. Ladéveze and J. Simmonds. De nouveaux concepts en théorie des poutres pour des charges et des géométries quelconques. *Comptes Rendus Acad. Sci. Paris*, 332:445–462, 1996.

[11] P. Ladevéze. *Nonlinear Computational Structural Mechanics*. Springer, 1999.

[12] B. Bognet, F. Bordeu, F. Chinesta, A. Leygue, and A. Poitou. Advanced simulation of models defined in plate geometries: 3d solutions with 2d computational complexity. *Computer Methods in Applied Mechanics and Engineering*, 201–204:1–12, 2012. doi: 10.1016/j.cma.2011.08.025.

[13] P. Vidal, L. Gallimard, and O. Polit. Composite beam finite element based on the proper generalized decomposition. *Computers and Structures*, 102–103:76–86, 2012. doi: 10.1016/j.compstruc.2012.03.008.

[14] V.L. Berdichevsky. Equations of the theory of anisotropic inhomogeneous rods. *Dokl. Akad. Nauk*, 228:558561, 1976.

[15] V.L. Berdichevsky, E. Armanios, and A. Badir. Theory of anisotropic thin-walled closed-cross-section beams. *Composites Engineering*, 2(5-7):411–432, 1992.

[16] V.V. Volovoi, D.H. Hodges, V.L. Berdichevsky, and V.G. Sutyrin. Asymptotic theory for static behavior of elastic anisotropic I-beams. *International Journal of Solid Structures*, 36(7):1017–1043, 1999.

[17] R. Schardt. Eine erweiterung der technischen biegetheorie zur berechnung prismatischer faltwerke. *Der Stahlbau*, 35:161–171, 1966.

[18] R. Schardt. *Verallgemeinerte technische biegetheorie*. Springer Verlag, 1989.

[19] N. Silvestre and D. Camotim. First-order generalised beam theory for arbitrary orthotropic materials. *Thin-Walled Structures*, 40(9):791–820, 2002.

[20] K. Washizu. *Variational Methods in Elasticity and Plasticity*. Pergamon, Oxford, 1968.

[21] K. Kapania and S. Raciti. Recent advances in analysis of laminated beams and plates, part I: Shear effects and buckling. *AIAA Journal*, 27(7):923–935, 1989.

[22] K. Kapania and S. Raciti. Recent advances in analysis of laminated beams and plates, part II: Vibrations and wave propagation. *AIAA Journal*, 27(7):935–946, 1989.

[23] E. Carrera, A. Pagani, M. Petrolo, and E. Zappino. Recent developments on refined theories for beams with applications. *Mechanical Engineering Reviews*, 2(2), 2015.

[24] E. Carrera, M. Cinefra, M. Petrolo, and E. Zappino. *Finite Element Analysis of Structures through Unified Formulation*. John Wiley & Sons, 2014.

[25] E. Carrera and A. Pagani. Analysis of reinforced and thin-walled structures by multi-line refined 1D/beam models. *International Journal of Mechanical Sciences*, 75:278–287, 2013. doi: 10.1016/j.ijmecsci.2013.07.010.

[26] E. Carrera, G. Giunta, P. Nali, and M. Petrolo. Refined beam elements with arbitrary cross-section geometries. *Computers and Structures*, 88(5–6):283–293, 2010. doi: 10.1016/j.compstruc.2009.11.002.

[27] S.M. Ibrahim, E. Carrera, M. Petrolo, and E. Zappino. Buckling of composite thin walled beams by refined theory. *Composite Structures*, 94(2):563–570, 2012. doi: 10.1016/j.compstruct.2011.08.020.

[28] A. Pagani, M. Boscolo, J. R. Banerjee, and E. Carrera. Exact dynamic stiffness elements based on one-dimensional higher-order theories for free vibration analysis of solid and thin-walled structures. *Journal of Sound and Vibration*, 332(23):6104–6127, 2013. doi: 10.1016/j.jsv.2013.06.023.

[29] E. Carrera and A. Varello. Dynamic response of thin-walled structures by variable kinematic one-dimensional models. *Journal of Sound and Vibration*, 331(24):5268–5282, 2012. doi: 10.1016/j.jsv.2012.07.006.

[30] E. Carrera and M. Petrolo. Refined one-dimensional formulations for laminated structure analysis. *AIAA Journal*, 50(1):176–189, 2012. doi: 10.2514/1.J051219.

[31] A. Pagani, E. Carrera, M. Boscolo, and J. R. Banerjee. Refined dynamic stiffness elements applied to free vibration analysis of generally laminated composite beams with arbitrary boundary conditions. *Composite Structures*, 110:305–316, 2014. doi: 10.1016/j.compstruct.2013.12.010.

[32] E. Carrera and M. Petrolo. On the effectiveness of higher-order terms in refined beam theories. *Journal of Applied Mechanics*, 78, 2011. doi: 10.1115/1.4002207.

[33] E. Carrera, A. Pagani, and M. Petrolo. Refined 1D finite elements for the analysis of secondary, primary and complete civil engineering structures. *Journal of Structural Engineering*, 2014. In Press, doi: 10.1061/(ASCE)ST.1943-541X.0001076.

[34] E. Carrera, F. Miglioretti, and M. Petrolo. Computations and evaluations of higher-order theories for free vibration analysis of beams. *Journal of Sound and Vibration*, 331:4269–4284, 2012. doi: 10.1016/j.jsv.2012.04.017.

[35] K.J. Bathe and E.N. Dvornik. A four node plate bending element based on mindlin-reissner plate theory and mixed interpolation. *International Journal of Numerical Methods in Engineering*, 21:367–383, 1985.

[36] K. J. Bathe. *Finite element procedure*. Prentice hall, 1996.

[37] P.-S. Lee, H.-C. Noh, and C.-K. Choi. Geometry-dependent mitc method for a 2-node iso-beam element. *Structural Engineering and Mechanics*, 29(2):203–221, 2008.

[38] E. Carrera and G. Giunta. Refined beam theories based on a unified formulation. *International Journal of Applied Mechanics*, 2(1):117–143, 2010. doi: 10.1142/S1758825110000500.

[39] E. Carrera, M. Petrolo, and P. Nali. Unified formulation applied to free vibrations finite element analysis of beams with arbitrary section. *Shock and Vibration*, 18:485–502, 2011. doi: 10.3233/SAV20100528.

[40] E. Carrera, G. Giunta, and M. Petrolo. *Beam Structures: Classical and Advanced Theories*. John Wiley & Sons, 2011. doi: 10.1002/9781119978565.

[41] S. W. Tsai. *Composites Design*. Dayton, Think Composites, 4th edition, 1988.

[42] J. N. Reddy. *Mechanics of laminated composite plates and shells. Theory and Analysis*. CRC Press, 2nd edition, 2004.

[43] E. Carrera and S. Brischetto. Analysis of thickness locking in classical, refined and mixed multilayered plate theories. *Composite Structures*, 82(4):549–562, 2008.

[44] P.-S. Lee, H.-C. Noh, and C.-K. Choi. Geometry-dependent MITC method or a 2-node iso-beam element. *Structural Engineering and Mechanics*, 29(2):203–221, 2008.

[45] A. Higdon, E. Ohlsen, W.B. Stiles, J.A. Weese, and W.F. Riley. *Mechanics of materials*. John Wiley & Sons, 4th edition edition, 1985.